

CrossMark  
click for updatesCite this: *Catal. Sci. Technol.*, 2016,  
6, 7163

# Electrochemically synthesized freestanding 3D nanoporous silver electrode with high electrocatalytic activity†

Lizhi Yuan,<sup>ac</sup> Luhua Jiang,<sup>\*a</sup> Tianran Zhang,<sup>a</sup> Guoxiong Wang,<sup>b</sup> Suli Wang,<sup>a</sup>  
Xinhe Bao<sup>b</sup> and Gongquan Sun<sup>\*a</sup>

Three-dimensional nanoporous metals of highly porous structure and interconnected ligaments are attractive for electrochemical reactions. Herein, freestanding 3D nanoporous silver (np-Ag) is prepared by a facile electrochemical approach, *i.e.*, first electro-oxidizing silver to silver halides followed by electro-reduction of the silver halides by controlling the potential applied to the electrode. The np-Ag displays 130 and 11.5 times enhancement in catalytic activity for the oxygen reduction reaction and the formaldehyde electro-oxidation reaction, respectively, relative to the flat polycrystalline silver, and even outperforms the commercial nano-Pt catalyst. Detailed experimental and theoretical studies discover that both the facilitated mass transportation in the 3D interconnected porous structures and the favored kinetics contribute to the superior electro-catalytic activity of np-Ag.

Received 31st May 2016,  
Accepted 7th July 2016

DOI: 10.1039/c6cy01174h

[www.rsc.org/catalysis](http://www.rsc.org/catalysis)

## Introduction

For heterogeneous electrocatalytic reactions, the construction of an effective electrode with both high intrinsic activity and facilitated mass transportation is crucial for practical application. Three-dimensional (3D) porous electrodes are therefore becoming more and more attractive.<sup>1–34</sup> For instance, replacing the planar electrode by the 3D carbon-based porous electrode enhances the discharging current of fuel cells by several orders of magnitude, profiting from the enlarged active surface of the 3D electrode. However, state-of-the-art carbon-based 3D porous electrodes suffer from (i) corrosion of carbon under working conditions and (ii) low catalyst utilization due to the binders at the interface partially covering the active surface. Freestanding porous metals are believed to be suitable materials for electrochemical reactions due to the continuously interconnected channels in metals and free of binders in electrodes. Recently, nanoporous silver (np-Ag) was reported to display equivalent ORR performance to that of the state-of-the-art nano-Pt catalyst,<sup>4</sup> and nanoporous gold was very active for CO<sub>2</sub> reduction.<sup>10</sup> Currently, most nanoporous metals are prepared by methods such as dealloying

protocol<sup>3,4,20,22,23,27,35–37</sup> and self-assembly,<sup>21,26</sup> template<sup>5</sup> and electrochemical methods.<sup>31,32,34,38</sup> Among them, the dealloying protocol is an important industrial process for preparing porous metals, such as RANEY® nickel.<sup>3</sup> However, the stringent and harsh multisteps of this process are also an inevitable problem. Except for the dealloying method, the electrochemical synthesis approaches are of distinct advantage in simplicity, economy and being environmentally benign are promising in large-scale synthesis. It has been reported that by simply applying a negative potential to a AgCl deposit layer, porous silver could be generated facilely.<sup>39</sup> Lately, nanoporous silver prepared by such an electrochemical approach was reported to be 32 times more active for CO<sub>2</sub> electro-reduction as compared to the flat silver sheet.<sup>6</sup> The electrochemically synthesized np-Ag might also be a promising candidate to replace Pt for ORR, the cathodic reaction of fuel cells. Furthermore, the formation mechanism of np-Ag prepared by the electrochemical approach has not been elucidated yet and the causes for its superior catalytic activity need to be understood.

In this work, we prepare a series of np-Ag starting from silver metal sheets by first electro-oxidizing Ag to AgCl and then electro-reducing AgCl to nanoporous Ag. Furthermore, we extend the intermediate from AgCl to other silver halides (AgBr, AgI) and confirm the generalization of the electrochemical approach. The electrocatalytic activity of np-Ag in the ORR is investigated. Moreover, the formation mechanism of the porous metals and the intrinsic causes for the superior catalytic activity are investigated and discussed, combining experimental and theoretical studies.

<sup>a</sup> Fuel Cell & Battery Division, Dalian National Laboratory for Clean Energy, Dalian Institute of Chemical Physics, Chinese Academy of Sciences, Dalian 116023, China. E-mail: [sunshine@dicp.ac.cn](mailto:sunshine@dicp.ac.cn), [gqsun@dicp.ac.cn](mailto:gqsun@dicp.ac.cn)

<sup>b</sup> State Key Laboratory of Catalysis, Dalian Institute of Chemical Physics, Chinese Academy of Sciences, Dalian 116023, China

<sup>c</sup> University of Chinese Academy of Sciences, Beijing 100039, China

† Electronic supplementary information (ESI) available. See DOI: 10.1039/c6cy01174h

## Experimental section

### Materials

Silver nitrate ( $\geq 99.8\%$ ), silver wire (0.2 mm diameter, 99.9%), and silver sheet (99.9%) were purchased from Sinopharm Chemical Reagent Co., Ltd.; Pt black was obtained from Johnson Matthey; diffusion layer was acquired from Toray Industries, Inc.; silver powder (*ca.* 100 nm) was obtained from Aladdin Industrial Chemical Reagent Co., Ltd.; sodium hydroxide ( $\geq 98\%$ ), sodium chloride ( $\geq 99.5\%$ ), sodium bromide ( $\geq 99\%$ ) and sodium iodide ( $\geq 99.5\%$ ) were obtained from Tianjin Damao Chemical Factory. All the chemicals were used without further purification. Deionized water ( $>18.2$  M $\Omega$  cm) was generated by a VEOLIA-ELGA Purelab Flex2 ultrapure water system.

### Synthesis of np-Ag

The np-Ag was synthesized in a three-electrode electrochemical cell (Scheme S1 $\dagger$ ) and the electrode potential was controlled by a CHI 760D electrochemical workstation. A silver sheet ( $1 \times 2$  cm $^2$ ) was used as the working electrode and a platinum sheet as the counter electrode. A Hg/HgO electrode in 0.1 M NaOH solution (denoted as MMO) acted as the reference electrode. All potentials in this work were calibrated and referred to a reversible hydrogen electrode (RHE). In a typical synthesis, the anodic oxidation of silver was carried out by applying a constant potential of 1.2 V to the silver sheet in an electrolyte solution containing both 0.1 M NaOH and 0.1 M NaCl for 2880 s. Then, the oxidized Ag sheet was reduced by applying a negative potential of 0.12 V to the silver sheet. After washing with water several times the obtained np-Ag was ready for use.

The procedure used for preparing all the other np-Ag was the same as that described above whether a smooth polycrystalline silver electrode (rotating disk electrode,  $\phi = 5$  mm) or a silver wire or silver powder (with an average Ag particle size of *ca.* 100 nm) was used as the starting material.

### Structural characterization

Scanning electron microscopy (SEM) images were obtained with a JEOL JSM 7800F microscope operating at an accelerating voltage of 3 kV. Transmission electron microscopy (TEM) images were taken using a JEOL JEM-2100 microscope at an accelerating voltage of 200 kV. X-ray diffraction (XRD) measurements were performed on a Rigaku X-2000 diffractometer using Cu K $\alpha$  radiation with a Ni filter. The tube voltage and the tube current were maintained at 40 kV and 100 mA, respectively. The sample was scanned from 15 $^\circ$  to 90 $^\circ$  ( $2\theta$ ) at a scan rate of 5 $^\circ$  min $^{-1}$ .

### Electrochemical measurements

Rotating disk electrode (RDE) tests were performed on an electrochemical workstation (CHI 760D, Chenhua Company). The preparation of the glassy carbon (5 mm in diameter) supported powder electrode is described as follows: 5.0 mg of

silver or platinum powder was dispersed in 175  $\mu$ L of ethanol and 25  $\mu$ L of 5 wt% Nafion $^\circledR$  solution (Du Pont) to form a well-dispersed ink. Then the ink (0.2  $\mu$ L, 6.5  $\mu$ L, 20.0  $\mu$ L, 37.6  $\mu$ L) was pipetted on a cleaned glassy carbon electrode and the solvent was evaporated at room temperature for about 10 min. Electrochemical experiments were carried out in a conventional three-electrode cell. Voltammetry experiments were performed in an O $_2$  or N $_2$  saturated 0.1 M NaOH solution at room temperature. The scan rate is 10 mV s $^{-1}$  and the rotation rate is 1600 rpm. A Pt wire was used as a counter electrode and a Hg/HgO electrode in 0.1 M NaOH solution (denoted as MMO) acted as a reference electrode. To evaluate the stability of the catalysts, an accelerated aging test (AAT) was conducted by running 1000 sweeps between 0.6 and 1.0 V with a scan rate of 100 mV s $^{-1}$  in an O $_2$  saturated 0.1 M NaOH aqueous solution at 25 $^\circ$ C.

## Results and discussion

### Preparation and characterization of np-Ag

As illustrated in Fig. 1a, the synthesis process involves two steps: first, anions are inserted (*e.g.*, Cl $^-$  ions) into the silver crystal lattice and then the anions were extracted from the AgCl crystals by controlling the electrode potential to generate freestanding 3D nanoporous silver (np-Ag). The high purity of both the AgCl intermediates and the final np-Ag are confirmed by both X-ray diffraction (XRD) (Fig. 1b) and elemental mapping analysis *via* EDS (Fig. S1 $\dagger$ ). The morphology of the starting Ag sheet, the AgCl intermediates and the np-Ag is characterized by SEM and displayed in Fig. 1c–e. The surface of the starting Ag sheet is rough with some scratches due to the mechanical polishing prior to the electrochemical treatment (Fig. 1c). The evolved AgCl intermediate domains with an average size at micrometer scale possess irregular shapes (Fig. 1d). At the boundary of the AgCl domains are distributed pores of hundreds of nanometers in size (denoted by white arrows in Fig. 1d), which are deduced to be the channels allowing Cl $^-$  ions in the electrolyte to be transported to the underlying Ag substrate and Ag $^+$  ions (obtained by oxidizing the pc-Ag substrate) from the Ag substrate to the electrolyte. The evolved np-Ag has a hierarchical porous structure (Fig. 1e). The primary porous structure originated from the boundary of the AgCl domains (Fig. 1d). Additionally, abundant secondary pores with tens of nanometers in size are generated on each domain (Fig. 1e), which are deduced to be the transport channels for Cl $^-$  ions escaping from the AgCl domains when a reduction potential was applied on the electrode.

To elucidate the formation mechanism of np-Ag, which is of both technical and scientific significance, we employed an *in situ* electrochemical technique and *ex situ* SEM characterization to monitor the nucleation and growth processes of the AgCl intermediate and nanoporous silver. For a typical Cl $^-$  insertion process ( $\text{Ag} + \text{Cl}^- \rightarrow \text{AgCl} + \text{e}^-$ ), as shown in Fig. S2a, $\dagger$  the oxidation current profile can be divided into two regions (regions I and II). In region I, *i.e.*, in the initial 100 s, the

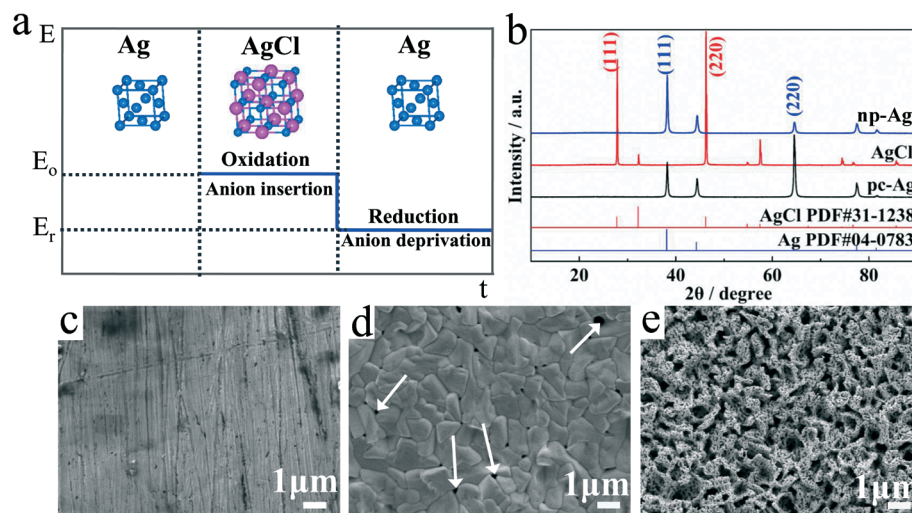


**Fig. 1** (a) Scheme of electrochemical preparation of nanoporous metals.  $E_o$  stands for the oxidation potential applied to the WE, at which silver is oxidized to AgCl and  $E_r$  stands for the reduction potential applied to the WE, at which AgCl is reduced to np-Ag. (b) The XRD patterns of the starting material: silver sheet (Ag), silver sheet after electro-oxidation (AgCl) and further electro-reduction (np-Ag). (c–e) SEM images of Ag (c), AgCl (d) and np-Ag (e).

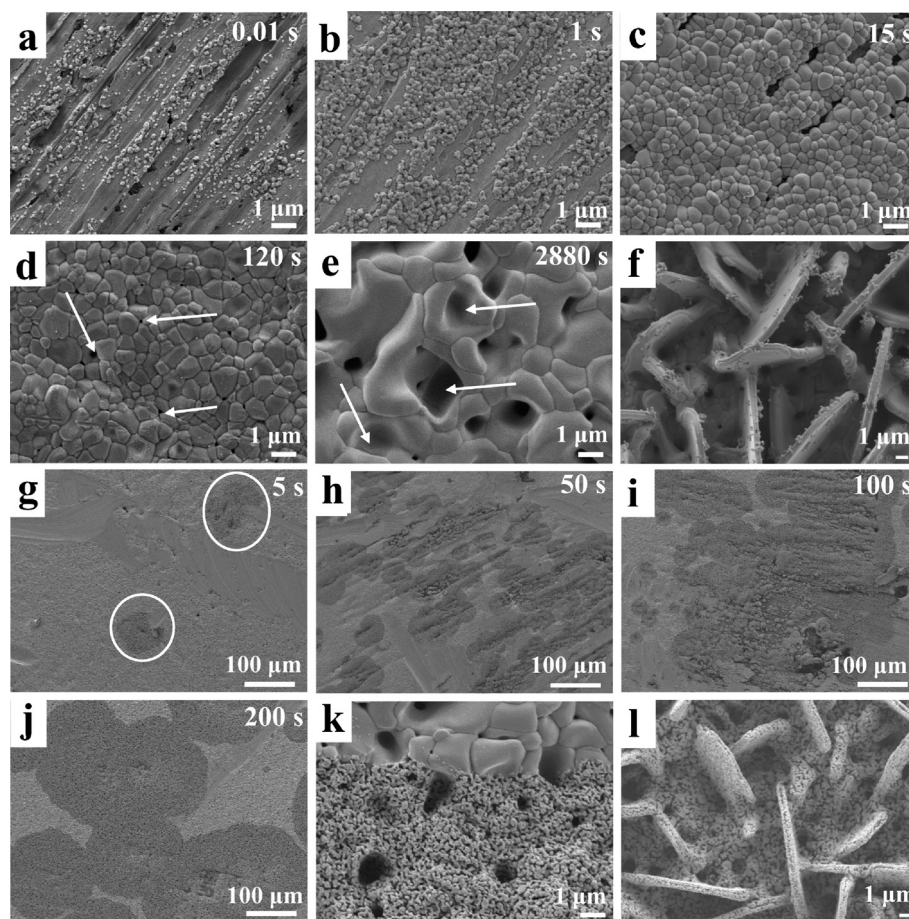


**Fig. 2** (a–e) SEM images of silver electrode after application of a potential of 1.2 V in 0.1 M NaOH and 0.1 M NaCl electrolyte for a certain time. (f) SEM image of AgCl obtained by applying a potential of 1.2 V to the silver electrode for 2880 s in 0.1 M NaOH + 3 M NaCl electrolyte. (g–j) SEM images of AgCl after application of a potential of 0.82 V for a certain time. (k) The enlarged SEM image of (i) displaying the interface of AgCl and np-Ag during the AgCl electro-reduction process. (l) SEM image of np-Ag obtained by applying a potential of 0.12 V to the AgCl in (f) for 100 s.

current decreased sharply from about 13.5 to 4.0 mA cm<sup>-2</sup>, which is named fast reaction region, implying that the initial Cl<sup>-</sup> insertion into the Ag lattice is a fast process due to the large solid-liquid interface between Ag and the electrolyte, generating a high concentration of Ag<sup>+</sup> ions at the Ag/electrolyte interface. The resultant Ag<sup>+</sup> ions form AgCl immediately once they meet the Cl<sup>-</sup> ions. In region II, which is named slow reaction region, the current tends gradually to be stable, probably due to the limited interface of Ag/electrolyte on the AgCl covered surface. Due to the fast insertion of Cl<sup>-</sup> ions in the silver crystal lattice, the preferential crystalline orientation of the AgCl, *i.e.*, AgCl (220) and AgCl (111), resembles that of its pc-Ag parents (Ag (220) and Ag (111)), as confirmed by XRD analysis (Fig. 1b), although AgCl (200) is normally the preferential orientation as shown at the bottom of Fig. 1b (PDF #04-0783). Furthermore, we analyzed the formation of AgCl domains by collecting the SEM images of the electrode in time. As shown in Fig. 2a, at 0.01 s after the oxidation potential is applied to the electrode, it was observed that the nucleation of AgCl is preferred at the ridge of the roughened silver surface probably due to the point discharging and the highly active unsaturated coordinated Ag atoms at the ridges. The generated AgCl then grew rapidly from around 150 nm to large domains of around 320 nm within 15 s to cover the Ag substrate (Fig. 2b and c). When the oxidation time is further prolonged to 120 s, only a few holes with irregular shapes of around 180 nm at the interface of the AgCl domains are left for ion transportation, as denoted by white arrows in Fig. 1d and 2d. This corresponds to region I (fast reaction) in Fig. S2a.† Continuously prolonging the oxidation time to 2880 s causes the AgCl domains to aggregate to form large islands with convex edges and concave centers, which evolve into dead-end holes, as denoted by the white arrows in Fig. 2e. The formation of the dead-end holes is the result of the coupling of the ion diffusion rate and the surface reaction rate. Specifically, the limited ion diffusion rate through the narrow channels leads to a high concentration of Ag<sup>+</sup> ions in the channels, which transform immediately to AgCl once Ag<sup>+</sup> ions diffuse out of the channels and meet Cl<sup>-</sup> ions; thus there is a low chance of Ag<sup>+</sup> ions diffusing farther to the center region of the AgCl domain. By prolonging the oxidation time, the AgCl domains continue to expand so that the inter-particle holes for ion transportation disappear. In this case, the Ag<sup>+</sup> ions can only diffuse out through the narrow gaps between the AgCl domains, which is also confirmed by the formation of AgCl walls obtained at a high Cl<sup>-</sup> concentration (3 M NaCl), as shown in the SEM image in Fig. 2f, due to the limited transportation rates of Ag<sup>+</sup> ions in the narrow interfacial channels. This corresponds to region II (slow reaction) in Fig. S2a.† It is therefore deduced that the potential-dependent ion diffusion rate and surface reaction rate determine the morphology of the AgCl intermediates.

For the AgCl reduction process ( $\text{AgCl} + \text{e}^- \rightarrow \text{Ag} + \text{Cl}^-$ ), the reaction occurs at the interface of Ag/AgCl/electrolytes. The reduction current profile shown in Fig. S2b† presents a para-

bolic curve. For the up-branch (the initial 120 s), the reduction current increases rapidly and then slowly to reach the maximum, suggesting the same reaction rate in this region. For the down-branch (120–310 s), the current first decreases slowly then sharply to zero. Correspondingly, from the SEM images (Fig. 2g–k), initially only small dark np-Ag patches appear around the large holes as denoted by the white circles in Fig. 2g. By prolonging the reduction time to 50 s, 100 s and 200 s, the np-Ag patches increase gradually in amount and extend around to connect to each other (Fig. 2h–j). Concurrently, the nanoporous structure of silver forms (Fig. 2k and l). Based on the above analysis, it is deduced that the Ag<sup>+</sup> ions in AgCl capture electrons very quickly and are reduced to Ag atoms driven by the cathodic potential; meanwhile, the Cl<sup>-</sup> ions were freed. The “phase” separation of Cl<sup>-</sup> anions and Ag atoms leads to a high concentration of Cl<sup>-</sup> anions and freed Ag atoms at the Ag/AgCl interface, far above their equilibration concentration, resembling the dealloying process of AuAg alloy.<sup>40</sup> That is, the system is inherently unstable and these silver atoms diffuse around and start to agglomerate into islands rather than forming a uniform silver layer, and as a result, exposing fresh AgCl surface to be reduced and leaving channels for Cl<sup>-</sup> ions diffusing out. It should be mentioned that the intrinsic difference between the electrochemical process and the chemical dealloying process lies in the driving force for the “phase separation” of two elements (here, Ag and Cl<sup>-</sup>). The electrochemical process studied herein is intrinsically governed by the electrochemical potential, while the dealloying process depends on the chemical potential of elements in alloys. From the above analysis, it is justified that the formation of the porous structure is governed by the rates of ion diffusion and surface reaction depending on the electrochemical potentials.

Since the porous structure is governed by the potential-dependent ion diffusion rate and surface reaction rate, it is possible to tune the sizes of the silver ligaments and pores of np-Ag by controlling the electrode potential. By varying the reduction potential applied to the AgCl intermediates from 0.82 to -0.88 V, the silver ligament size of np-Ag can be tuned from 166 to 36 nm and the pore size can be varied from 155 to 28 nm, as shown in Fig. 3. It is clear that a high overpotential generates small silver ligaments and pores, which is reasonable since the overpotential stands for the driving force for electrochemical reactions. The larger the overpotential, the faster the electrochemical reaction rates, thus generating more crystalline seeds simultaneously. On the contrary, with lower overpotentials, the electrochemical reduction rate is slower and the silver ligaments grow larger. By altering the time of the anodic oxidation from 120 to 5760 s, the thickness of the np-Ag layer can be controlled from 3.2 to 32.5 μm (Fig. 4 and Table S1†).

This approach to prepare nanoporous silver is versatile, *i.e.*, the substrate can be extended from bulk silver sheet to silver powder and silver wire, as shown in the SEM images displayed in Fig. S3.† Furthermore, using alternative anions

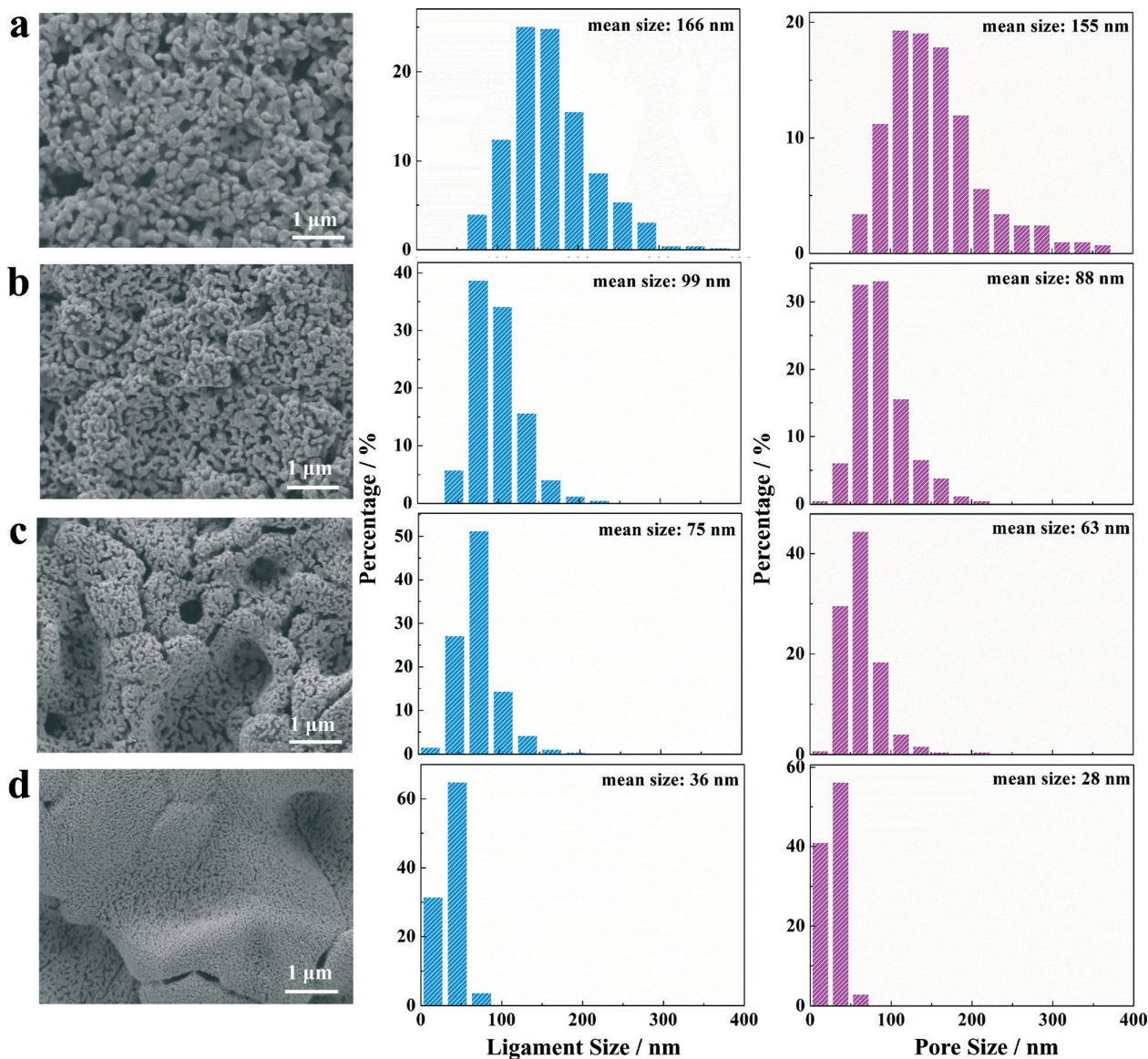


**Fig. 3** SEM images of np-Ag and size histograms of the corresponding Ag ligaments and secondary pores of np-Ag. The np-Ag synthesized at the oxidation potential of 1.2 V followed by reduction at a potential of 0.82 V (a), 0.12 V (b), -0.68 V (c), and -0.88 V (d) in 0.1 M NaCl and 0.1 M NaOH electrolyte.

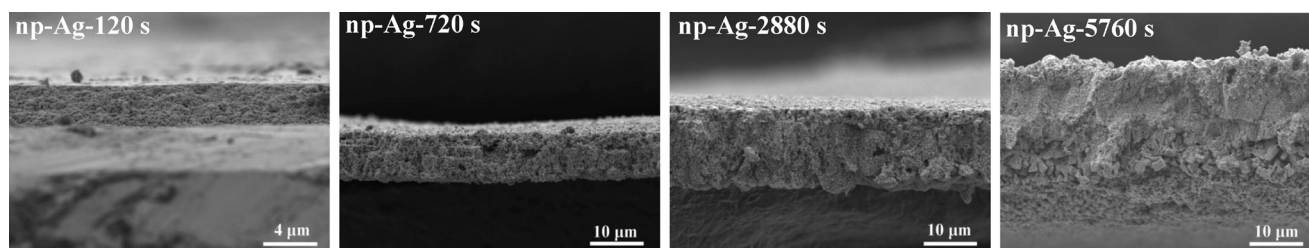


**Fig. 4** SEM images of a cross section of np-Ag obtained at different oxidation times.

in the electrolyte, such as  $\text{Br}^-$  and  $\text{I}^-$ , we can also obtain np-Ag of different morphologies (Fig. S4<sup>†</sup>). This approach is also easily scaled up depending on the size of the starting metal.

Fig. S5<sup>†</sup> displays np-Ag with a size of  $3 \times 5 \text{ cm}^2$ , which makes it attractive to act as a freestanding electrode for electrochemical devices.

## Electrochemical performance of np-Ag

The electrochemically generated 3D free-standing interconnected porous structure endows np-Ag with merits including (i) facilitated diffusion within the interconnected porous network; (ii) large effective surface owing to the binder-free structure; (iii) excellent electronic conductivity due to the continuous metals; (iv) fresh, thus active, surface exposed to reactants. These merits suggest a potential extensive application of np-Ag in electro-catalytic reactions.

Herein, oxygen reduction reaction (ORR), the cathodic reaction of fuel cells, is used as the main probing reaction to investigate the electro-catalytic activity of np-Ag. Commercial 100 nm Ag powder (Aladdin, similar size to the ligaments of np-Ag), 8 nm Pt black (Johnson Matthey) and smooth polycrystalline silver (pc-Ag) were used for comparison. From the ORR polarization curves (Fig. 5a), the half-wave potential ( $E_{1/2}$ ) of the ORR for np-Ag is  $\sim 232$  and 82 mV more positive than that for the pc-Ag and Ag powder, respectively, and more surprisingly, it is even 23 mV more positive than that for the commercial nano-Pt, suggesting the superior catalytic activity of np-Ag for the ORR. Specifically, the ORR current density at 0.9 V is 2.897 mA cm<sup>-2</sup> with np-Ag as the electrocatalyst, which is about 130 times higher than that with pc-Ag (0.022 mA cm<sup>-2</sup>). The ORR performance of np-Ag is compared with those reported in the literature and listed in Table S2.† The np-Ag displays the highest catalytic activity among all the reported Ag-based catalysts.

To meet the requirements for practical applications, we evaluated the stability of the np-Ag electrocatalyst *via* an electrochemical accelerated aging test (AAT). After 1000 potential cycles from 0.6 to 1.0 V, the ORR half-wave potential for np-Ag shifts 20 mV negatively, as observed in Fig. S6,† which is similar to that for most of the reported Pt catalysts.<sup>41</sup> Further investigation reveals that the loss in activity of np-Ag is mainly caused by the reduced ECSA (Fig. S7g and Table S1†) due to the coarsened Ag ligaments after the AAT as characterized by SEM (Fig. S8d–f†). Delightfully, the aged samples can be easily regenerated electrochemically *via* the same process as it was obtained. After regeneration,

the Ag ligament size (Fig. S8g–i†) and thus the ECSA of the np-Ag are restored (Fig. S7h and Table S1†). The ORR activity of the regenerated np-Ag is recovered (Fig. S6 and Table S1†). The facile regeneration process makes this novel approach more attractive for practical application.

The np-Ag also displays superior catalytic activity to the formaldehyde electro-oxidation reaction (FOR) (Fig. 5b). From the FOR polarization curves, the onset potential ( $E_{\text{onset}}$ ) for the FOR on the np-Ag (0.063 V) is more negative than that on its counterparts (0.333 V for pc-Ag, 0.285 V for nano-Pt black and 0.114 V for nano-Ag powder). Specifically, the FOR current density at 0.4 V is 93.8 mA cm<sup>-2</sup> with np-Ag as the electrocatalyst, which is about 11.3, 6.7, and 1.8 times higher than that with pc-Ag (8.3 mA cm<sup>-2</sup>), nano-Pt black (14.0 mA cm<sup>-2</sup>) and nano-Ag powder (51.0 mA cm<sup>-2</sup>) as the catalysts, respectively.

The superior performance of np-Ag stimulates us to discover the intrinsic causes for the high catalytic activity. First of all, considering that np-Ag possesses a unique 3D porous structure, the mass transportation in such a structure is believed to be superior to that of the powder catalysts. We thus comparatively investigated the influence of the mass of both np-Ag and 100 nm Ag powder on the ORR activity, as shown in Fig. S9.† For a parallel comparison, equivalent amounts of Ag powder and np-Ag were used for each group (see Table S1† for the calculation method of the mass of np-Ag). The  $E_{1/2}$  of the ORR were collected and displayed in Fig. 6a. This reveals that the  $E_{1/2}$  of the ORR shifts positively from 0.75 to 0.90 V with increasing mass of Ag from  $5.1 \times 10^{-3}$  to 0.940 mg for np-Ag (corresponding to 3.2 to 14.5  $\mu\text{m}$  in thickness). In contrast, for the Ag powder, the  $E_{1/2}$  only increases from 0.69 to 0.80 V with increasing mass of Ag from  $5.1 \times 10^{-3}$  to 0.162 mg, and further increase in the Ag mass cannot improve the ORR activity. This implies that the mass transportation in the np-Ag, benefiting from its interconnected porous structure, is facilitated compared to that in the Ag powder. To confirm this, the electrochemical surface areas (ECSAs) of np-Ag and 100 nm-Ag powder were evaluated *via* the Pb<sub>UPD</sub> charges<sup>42,43</sup> (see Fig. S7†) as a function of the mass of Ag (*i.e.*, the thickness of the Ag layer) and displayed

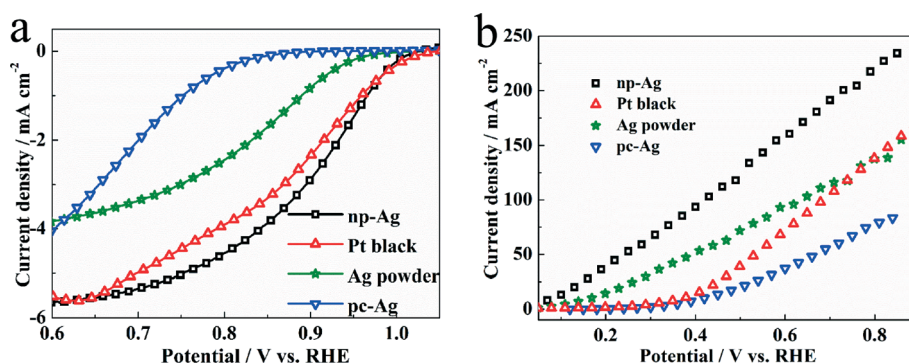


Fig. 5 (a) ORR polarization curves measured in oxygen-saturated 0.1 M NaOH electrolyte (rotation rate: 1600 rpm, scan rate: 10 mV s<sup>-1</sup>); (b) formaldehyde electrooxidation polarization curves measured in N<sub>2</sub> saturated 0.1 M NaOH solution containing 0.1 M HCHO (scan rate: 10 mV s<sup>-1</sup>). The np-Ag, Ag powder and Pt black are of the same metal loading (0.94 mg).

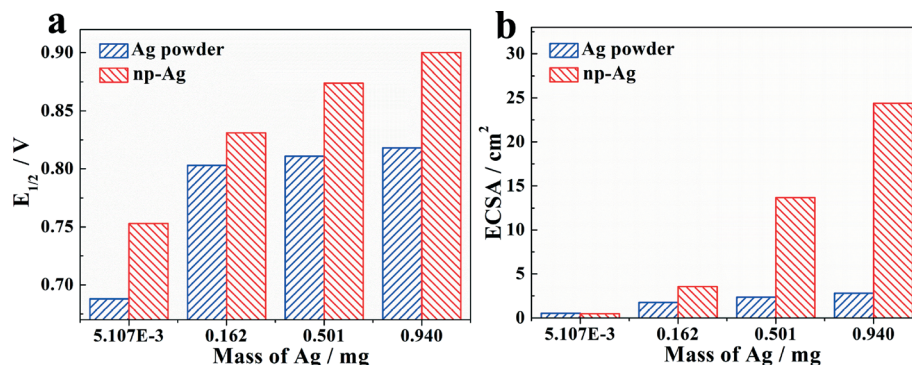


Fig. 6 ORR catalytic activity (a) and ECSA (b) histogram of np-Ag catalysts with different oxidation time and corresponding Ag powder catalysts with the same quantity.

in Fig. 6b. For the np-Ag, the ECSA increases almost linearly with the Ag mass, while for the 100 nm Ag powder, the ECSA increases with the Ag mass to 0.162 mg and then remains almost constant with further increase in the Ag mass. It is noted that the trends of the ORR catalytic activity with the increased Ag mass for both Ag powder and np-Ag catalysts are parallel to the trends of the ECSA, suggesting that the improved ORR activity is related with the enlarged ECSA. With the increase in the Ag thickness, the 3D continuous nanoporous structure of np-Ag facilitates the mass transportation in the electrode, as reflected by the continuous increase in active surface area with the Ag mass (Table S1†). In contrast, for the powder catalysts, *i.e.*, Ag powder and Pt powder, the metal powder adhered together *via* binders, which brings two adverse aspects. One is fewer active sites due to the stacking structure of metal particles and the other is the adverse mass transportation in electrodes due to the stacking structure and the binders between particles.

Except for the advantage in mass transportation of np-Ag, the intrinsic activity of the unique Ag surface in the ORR is also intriguing. In the HRTEM image of np-Ag, as shown in Fig. S10,† considerable step sites on the np-Ag surface were observed, which may influence the ORR catalytic activity. Although silver single crystal facets are intrinsically less active for the ORR than platinum single crystal facets due to the weak adsorption of oxygen on silver from both DFT calculations and experimental results,<sup>44</sup> np-Ag with a large amount of step sites on the surface brings about different results, since Ag step sites with lower coordination may improve the ability to donate electrons to oxygen and thus are more energetically favorable for oxygen adsorption. The DFT calculations on the ORR process on step sites and the perfect surface of silver are compared (see the ESI† for details). Two of the most stable surfaces, Ag (001) surface and Ag (111) surface, are employed as the computing models and the step sites are constructed by removing several rows of atoms on the top two layers (inset of Fig. S11b†). Considering that the binding energies of O and OH ( $\Delta E_{\text{O}}$  and  $\Delta E_{\text{OH}}$ ) on the surface

are important descriptors for the ORR,<sup>45</sup> we calculated and compared  $\Delta E_{\text{O}}$  and  $\Delta E_{\text{OH}}$  on the stepped and perfect surfaces (see the ESI† for details). Fig. S11a† shows the trends in ORR activity as a function of both  $\Delta E_{\text{O}}$  and  $\Delta E_{\text{OH}}$ , which is plotted according to ref. 45. It is obvious that for both Ag (111) and Ag (001) surfaces, the stepped surface is much more active than the perfect one with smaller  $\Delta E_{\text{O}}$  or larger  $\Delta E_{\text{OH}}$ , possibly attributed to the stronger electron-donating ability of the edge atoms at the steps. It is noteworthy that  $\Delta E_{\text{O}}$  and  $\Delta E_{\text{OH}}$  for the stepped Ag surfaces locate in the same region as those for the Pt surface in Fig. S11a,† demonstrating the comparable activity of the stepped Ag surface to that of the benchmark Pt surface. To further confirm the results, the intermediates (Fig. S12†) involved in the ORR and corresponding free-energy path (Fig. S11b†) are calculated on the constructed surfaces. As shown in Fig. S11b,† at the equilibrium potential ( $U = 1.23$  eV), the performances of the stepped Ag surfaces and the perfect Ag surfaces during the  $4e^-$  reduction process are limited by the reduction of  $\text{O}_2$  to OOH, similar to that on the Pt surfaces. The energy required to form OOH on the stepped Ag surfaces is less than that on the perfect Ag surface and is equal to that on the Pt surface, indicating that the stepped surface facilitates  $\text{O}_2$  reduction and OOH formation, resulting in a similar activity of the stepped Ag to that of Pt. The DFT calculations provide evidence that the step sites over the Ag surface are highly active to the reduction of oxygen.

## Conclusions

In conclusion, 3D freestanding nanoporous silver was synthesized *via* a versatile and effective template-free electrochemical approach. This approach involves inserting anions (*e.g.*,  $\text{Cl}^-$ ,  $\text{Br}^-$ ,  $\text{I}^-$ ) into the silver crystal lattice to form insoluble deposits and subsequently extracting the anions from the deposits by controlling the electrode potential. Governed by the potential-dependent ion diffusion rate and surface reaction rate, the pore size and silver ligament size of the np-Ag can be easily tuned. The np-Ag displays 130 and 11.5 times

enhancement in catalytic activity to oxygen reduction reaction and formaldehyde electro-oxidation reaction, respectively, relative to the flat polycrystalline silver, and even outperforms the commercial nano-Pt catalyst. The facilitated mass transportation in the 3D interconnected porous structures, confirmed by the increase in ECSA with increasing thickness of the porous structure, together with the favorable formation of the OOH intermediate (rate-determining step) on the stepped sites of the np-Ag surface revealed by the DFT calculations and the high electronic conductivity of the three-dimensional metal network all contribute to the superior electro-catalytic activity of np-Ag.

## Acknowledgements

The authors acknowledge financial support from the Key Programme of the Chinese Academy of Sciences (Grant No. KGZD-EW-T08), the National Basic Research Program of China (973 Program, Grant No. 2012CB215500) and the Strategic Priority Research Program of the Chinese Academy of Sciences (Grant No. XDA09030104).

## References

- X. Zhang and Y. Ding, *Catal. Sci. Technol.*, 2013, 3, 2862–2868.
- M. Hakamada, F. Hirashima and M. Mabuchi, *Catal. Sci. Technol.*, 2012, 2, 1814–1817.
- M. Raney, Method of producing Finely Divided Nickel, *US Pat.*, 1628190, issued 1927-05-10, 1927.
- Y. Zhou, Q. Lu, Z. Zhuang, G. S. Hutchings, S. Kattel, Y. Yan, J. G. Chen, J. Q. Xiao and F. Jiao, *Adv. Energy Mater.*, 2015, 5, DOI: 10.1002/aenm.201500149.
- C. Li, Ö. Dag, T. D. Dao, T. Nagao, Y. Sakamoto, T. Kimura, O. Terasaki and Y. Yamauchi, *Nat. Commun.*, 2015, 6, 6608.
- Y.-C. Hsieh, S. D. Senanayake, Y. Zhang, W. Xu and D. E. Polyansky, *ACS Catal.*, 2015, 5349–5356.
- A. Wittstock and M. Bäumer, *Acc. Chem. Res.*, 2014, 47, 731–739.
- S. Sen, D. Liu and G. T. R. Palmore, *ACS Catal.*, 2014, 4, 3091–3095.
- C. W. Li and M. W. Kanan, *J. Am. Chem. Soc.*, 2012, 134, 7231–7234.
- Y. Chen, C. W. Li and M. W. Kanan, *J. Am. Chem. Soc.*, 2012, 134, 19969–19972.
- L. Zhang, L. Chen, H. Liu, Y. Hou, A. Hirata, T. Fujita and M. Chen, *J. Phys. Chem. C*, 2011, 115, 19583–19587.
- X. Xing, S. Cherevko and C.-H. Chung, *Mater. Chem. Phys.*, 2011, 126, 36–40.
- J.-L. Shui, C. Chen and J. C. M. Li, *Adv. Funct. Mater.*, 2011, 21, 3357–3362.
- A. Ott, L. A. Jones and S. K. Bhargava, *Electrochem. Commun.*, 2011, 13, 1248–1251.
- S. Cherevko and C.-H. Chung, *Electrochem. Commun.*, 2011, 13, 16–19.
- T. Chen, Z. Liu, W. Lu, X. Zhou and H. Ma, *Electrochem. Commun.*, 2011, 13, 1086–1089.
- C. Xu, Y. Li, F. Tian and Y. Ding, *ChemPhysChem*, 2010, 11, 3320–3328.
- A. Wittstock, V. Zielasek, J. Biener, C. M. Friend and M. Bäumer, *Science*, 2010, 327, 319–322.
- B. C. Tappan, S. A. Steiner and E. P. Luther, *Angew. Chem., Int. Ed.*, 2010, 49, 4544–4565.
- J. Snyder, T. Fujita, M. W. Chen and J. Erlebacher, *Nat. Mater.*, 2010, 9, 904–907.
- K. S. Krishna, C. S. S. Sandeep, R. Philip and M. Eswaramoorthy, *ACS Nano*, 2010, 4, 2681–2688.
- L.-Y. Chen, J.-S. Yu, T. Fujita and M.-W. Chen, *Adv. Funct. Mater.*, 2009, 19, 1221–1226.
- J. Yu, Y. Ding, C. Xu, A. Inoue, T. Sakurai and M. Chen, *Chem. Mater.*, 2008, 20, 4548–4550.
- Y. Sun and T. J. Balk, *Scr. Mater.*, 2008, 58, 727–730.
- R. Klajn, T. P. Gray, P. J. Wesson, B. D. Myers, V. P. Dravid, S. K. Smoukov and B. A. Grzybowski, *Adv. Funct. Mater.*, 2008, 18, 2763–2769.
- M. Kim, G. H. Jeong, K. Y. Lee, K. Kwon and S. W. Han, *J. Mater. Chem.*, 2008, 18, 2208–2212.
- C. Xu, J. Su, X. Xu, P. Liu, H. Zhao, F. Tian and Y. Ding, *J. Am. Chem. Soc.*, 2007, 129, 42–43.
- Y. Li, Y.-Y. Song, C. Yang and X.-H. Xia, *Electrochem. Commun.*, 2007, 9, 981–988.
- Y. Li, W.-Z. Jia, Y.-Y. Song and X.-H. Xia, *Chem. Mater.*, 2007, 19, 5758–5764.
- F. Jia, C. Yu, Z. Ai and L. Zhang, *Chem. Mater.*, 2007, 19, 3648–3653.
- H. C. Shin and M. Liu, *Adv. Funct. Mater.*, 2005, 15, 582–586.
- H. C. Shin, J. Dong and M. Liu, *Adv. Mater.*, 2004, 16, 237–240.
- Y. Ding, M. Chen and J. Erlebacher, *J. Am. Chem. Soc.*, 2004, 126, 6876–6877.
- H. C. Shin, J. Dong and M. Liu, *Adv. Mater.*, 2003, 15, 1610–1614.
- Q. Lu, J. Rosen, Y. Zhou, G. S. Hutchings, Y. C. Kimmel, J. G. Chen and F. Jiao, *Nat. Commun.*, 2014, 5.
- T. Fujita, P. Guan, K. McKenna, X. Lang, A. Hirata, L. Zhang, T. Tokunaga, S. Arai, Y. Yamamoto, N. Tanaka, Y. Ishikawa, N. Asao, Y. Yamamoto, J. Erlebacher and M. Chen, *Nat. Mater.*, 2012, 11, 775–780.
- Z. Qi, U. Vainio, A. Kornowski, M. Ritter, H. Weller, H. Jin and J. Weissmüller, *Adv. Funct. Mater.*, 2015, 25, 2530–2536.
- S. Cherevko, X. Xing and C.-H. Chung, *Electrochem. Commun.*, 2010, 12, 467–470.
- X. Jin, J. Lu, P. Liu and H. Tong, *J. Electroanal. Chem.*, 2003, 542, 85–96.
- J. Erlebacher, M. J. Aziz, A. Karma, N. Dimitrov and K. Sieradzki, *Nature*, 2001, 410, 450–453.
- Q. Tang, L. Jiang, J. Qi, Q. Jiang, S. Wang and G. Sun, *Appl. Catal., B*, 2011, 104, 337–345.

- 42 G. K. H. Wiberg, K. J. J. Mayrhofer and M. Arenz, *Fuel Cells*, 2010, **10**, 575–581.
- 43 G. Wiberg, K. Mayrhofer and M. Arenz, *ECS Trans.*, 2009, **19**, 37–46.
- 44 Y. Lei, F. Mehmood, S. Lee, J. Greeley, B. Lee, S. Seifert, R. E. Winans, J. W. Elam, R. J. Meyer, P. C. Redfern, D. Teschner, R. Schlögl, M. J. Pellin, L. A. Curtiss and S. Vajda, *Science*, 2010, **328**, 224–228.
- 45 J. K. Nørskov, J. Rossmeisl, A. Logadottir, L. Lindqvist, J. R. Kitchin, T. Bligaard and H. Jónsson, *J. Phys. Chem. B*, 2004, **108**, 17886–17892.